"Capillary pinch-off in inviscid fluids"

by

David Leppinen & John R. Lister

Department of Applied Mathematics and Theoretical Physics

University of Cambridge

Silver Street, Cambridge CB3 9EW, United Kingdom

Abstract: The axisymmetric pinch-off of an inviscid drop of density ρ_1 immersed in an ambient fluid of density ρ_2 is examined over a range of the density ratio $D = \rho_2/\rho_1$. For moderate values of D, time-dependent simulations based on a boundary-integral representation show that inviscid pinch-off is asymptotically self-similar with length scales decreasing like $\tau^{2/3}$ and velocities increasing like $\tau^{-1/3}$, where τ is the time to pinch-off. The similarity equations are solved directly using a modified Newton's method and continuation on D to obtain a branch of similarity solutions for $0 \leq D \leq 11.8$. All solutions have a double-cone interfacial shape with one of the cones folding back over the other in such a way that its internal angle is greater than $90°$. Bernoulli suction due to a rapid internal jet from the narrow cone into the folded-back cone plays a significant role near pinching. The similarity solutions are linearly stable for $0 \leq D \leq 6.2$ and unstable to an oscillatory instability for $D \geq 6.2$. Oscillatory behaviour is also seen in the approach to self-similarity in the time-dependent calculations. Further instabilities are found as D increases and the steady solution branch is lost at a stationary bifurcation at $D = 11.8$.

1

1   Introduction

Capillary-driven pinch-off of free surface flows has been the subject of a considerable amount of recent research. By pinch-off we refer to the process by which a single drop breaks up into two or more drops, or where a jet of one fluid, passing into another fluid, disintegrates into a series of drops. Common examples of pinch-off include water dripping from a tap and the formation of drops during ink-jet printing. Pinch-off in viscous fluids has been studied by [1, 2, 3], while pinch-off in inviscid fluids has been studied by [4, 5], An extensive review is given by Eggers [6].

Pinch-off is an example of a process which exhibits a finite-time singularity: both the interfacial curvature and the interfacial velocity diverge to infinity as the time until pinch-off approaches zero. As pinch-off is approached, the relevant length and time scales become orders of magnitude smaller than any externally imposed length and time scales. Consequently, we expect pinch-off to be independent of the initial conditions and any external forcing, and thus to evolve self-similarly in time. The purpose of this paper is to examine the self-similar pinch-off of an inviscid drop of density ρ_1, immersed in an inviscid ambient fluid of density ρ_2, in order to investigate the effect of the density ratio $D = \rho_2/\rho_1$. The particular cases of $D = 0$ and $D = 1$ have been examined by Day, Hinch and Lister [4] and Chen & Steen [5] respectively.

This paper is organized as follows. In section 2 we introduce a mathematical description of the problem based on a boundary-integral representation, which is used to examine the surface-tension-driven evolution of an inviscid drop in an otherwise quiescent environment. Our numerical implementation of the time-dependent equations is described and the numerical scheme is validated against known analytical results. Data from time-dependent simulations in section 3 are re-scaled to show that pinch-off is an asymptotically self-similar phenomenon. In sections 4 and 5 the mathematical description is re-formulated in terms of similarity variables, and similarity solutions are obtained using a modified Newton iteration scheme for a range of density ratios. Stability analysis of the similarity solutions is used to interpret the time-dependent results in section 6 and conclusions are presented in section 7.

2 Mathematical formulation

We consider a finite drop of internal fluid of density $\rho = \rho_1$ surrounded by an external fluid of density $\rho = \rho_2$. The two fluids are incompressible, inviscid and immiscible, and the closed surface of the drop, S, has unit outward normal $\mathbf{n}$ and constant surface tension σ. If the flow in the internal and external fluids is assumed to be irrotational, then the velocity $\mathbf{u}$ can be written as $\mathbf{u} = \nabla\phi$, where the velocity potential ϕ satisfies

$$\nabla^2 \phi = 0. \tag{1}$$

The kinematic boundary condition requires the fluid velocity to have a normal component that is continuous across the surface S and equal to the normal velocity of the interface $\mathbf{n} \cdot \mathbf{u}$;

$$\mathbf{n} \cdot \mathbf{u} = (\mathbf{n} \cdot \nabla\phi)^- = (\mathbf{n} \cdot \nabla\phi)^+ , \tag{2}$$

where the superscript $+$ $(-)$ is used to denote quantities evaluated just external (internal) to S. By combining the Bernoulli equation for each fluid with the Young–Laplace equation, the normal-stress balance across S is given by

$$\rho_1 \left(\frac{\partial\phi}{\partial t} + \frac{1}{2} |\nabla\phi|^2 \right)^- - \rho_2 \left(\frac{\partial\phi}{\partial t} + \frac{1}{2} |\nabla\phi|^2 \right)^+ + \kappa\sigma = 0 , \tag{3}$$

where $\kappa = \nabla \cdot \mathbf{n}$ is the mean curvature of the interface. The external fluid is assumed to be at rest at infinity.

Eqs. (1)–(3) specify a potential-flow problem which we non-dimensionalize using a length scale L (e.g. the characteristic size of the drop), time scale $(\rho_1 L^3/\sigma)^{1/2}$ and velocity-potential scale $(\sigma L/\rho_1)^{1/2}$. The Bernoulli condition becomes

$$\left(\frac{\partial\phi}{\partial t} + \frac{1}{2} |\nabla\phi|^2 \right)^- - D \left(\frac{\partial\phi}{\partial t} + \frac{1}{2} |\nabla\phi|^2 \right)^+ + \kappa = 0 , \tag{4}$$

where all variables are now dimensionless and $D = \rho_2/\rho_1$ is the ratio of the external density to the internal density.

According to classical potential-flow theory, the velocity potential can be written in terms of a dipole distribution on S of strength μ, with

$$\phi(\mathbf{x}) = \int_S \mu(\mathbf{x}') \, \mathbf{n} \cdot \nabla_{\mathbf{x}'} G(\mathbf{x}, \mathbf{x}') \, dS' , \tag{5}$$

3

where $G(\mathbf{x}, \mathbf{x}') = -(4\pi|\mathbf{x} - \mathbf{x}'|)^{-1}$ is the free-space Green's function for Laplace's equation. There is a jump in $\phi(\mathbf{x})$ across S with

$$\phi^- = \overline{\phi} + \frac{1}{2}\mu \tag{6}$$

$$\phi^+ = \overline{\phi} - \frac{1}{2}\mu , \tag{7}$$

where $\overline{\phi}$ denotes the velocity potential on S as evaluated using (5). The jump in $\phi(\mathbf{x})$ across S is associated with a jump in the tangential velocity across S. In our numerical scheme, material points on S are advected according to

$$\frac{d\mathbf{x}}{dt} = \nabla\overline{\phi} , \tag{8}$$

where the normal derivative is given the obvious meaning (2) and the tangential derivative gives the average of the tangential velocities on either side of S.

The evolution of μ is determined by manipulation of Eqs. (4)–(7). In particular, Eq. (4) can be rewritten as

$$\frac{d\beta}{dt} = \nabla\phi^- \cdot \left(\nabla\overline{\phi} - \frac{1}{2}\nabla\phi^-\right) - D\nabla\phi^+ \cdot \left(\nabla\overline{\phi} - \frac{1}{2}\nabla\phi^+\right) - \kappa , \tag{9}$$

where

$$\beta = \phi^- - D\phi^+ = (1 - D)\overline{\phi} + \frac{1}{2}(1 + D)\mu \tag{10}$$

and $\frac{d}{dt} = \frac{\partial}{\partial t} + \nabla\overline{\phi}\cdot\nabla$ is the total time derivative following the material points on S. Rewriting Eq. (5) symbolically as $\phi = I[\mu]$, it follows that

$$\beta = (1 - D)I[\mu] + \frac{1}{2}(1 + D)\mu , \tag{11}$$

which is an integral equation that can be inverted for μ given β. For the special case $D = 1$, it is not necessary to invert an integral equation since $\beta = \mu$.

2.1 Numerical scheme for time-dependent simulations

For simplicity, only axisymmetric flows are considered so that the surface S can be thought of as generated by the rotation of a curve C about the Z-axis of the R–Z plane in cylindrical polar coordinates (see Fig. 1). The surface velocity in Eq. (8) is decomposed as

$$\frac{d\mathbf{x}}{dt} = \frac{\partial\overline{\phi}}{\partial s}\mathbf{t} + \frac{\partial\overline{\phi}}{\partial n}\mathbf{n} , \tag{12}$$

4

where $\mathbf{t}$ is the unit tangent vector and $\partial\overline{\phi}/\partial s$ and $\partial\overline{\phi}/\partial n$ are the tangential and normal derivatives of $\overline{\phi}$ respectively. The tangential velocity $\partial\overline{\phi}/\partial s$ is obtained directly by differentiation of $\overline{\phi}$ as calculated using Eq. (5). Following Nie & Baker [7], the normal velocity $\partial\overline{\phi}/\partial n$ is calculated from

$$\frac{\partial\overline{\phi}}{\partial n} = \mathbf{n} \cdot (\nabla \wedge \mathbf{A}) , \tag{13}$$

where the associated velocity potential $\mathbf{A}$ is given by

$$\mathbf{A}(\mathbf{x}) = \int_S \mu(\mathbf{x}')\mathbf{n}(\mathbf{x}') \wedge \nabla_{\mathbf{x}'}G(\mathbf{x},\mathbf{x}') \, dS'. \tag{14}$$

Eqs. (13) and (14) allow $\partial\overline{\phi}/\partial n$ to be calculated using only information on S. The azimuthal integrations in the surface integrals (5) and (14) are performed analytically, as in [7], so that the surface integrals are reduced to line integrals.

The interface is discretized using N_p Lagrangian points at $\mathbf{x}_i(t)$ ($i = 1, 2, \ldots, N_p$) with dipole strengths $\mu_i(t)$. Quintic splines based on arclength are used to interpolate between the nodal points. The line integrals left after azimuthal integration are performed using 16-point Gaussian quadrature on each panel between adjacent nodes. Eqs. (8) and (9) are marched forward in time using a fourth-order Runge-Kutta scheme. The accuracy of the numerical scheme was verified by comparison with analytical results, as described in the Appendix.

In order to resolve the short time and length scales near pinch-off, adaptive re-gridding was applied at the beginning of each time step with the local grid spacing set proportional to the distance of each grid point from the point $(Z_{\min}, 0)$, where $(Z_{\min}, R_{\min})$ is the location of the minimum neck radius once such a minimum has developed. Additional grid-points were added whenever $\Delta s_{\min}/R_{\min}$ exceeded 0.1, where $\Delta s_{\min}$ is the minimum spacing between nodes. Adaptive time-stepping was employed with $\Delta t = 0.2\Delta s_{\min}^{3/2}$.

3   Time-dependent simulations of pinch-off

A series of simulations were performed using initial conditions of a highly deformed droplet released from rest which then evolved under the action of surface tension. For some initial shapes, the drops would undergo large-scale deformations but would oscillate indefinitely without breaking up. For other initial shapes, pinch-off would occur with the initial drop

5

breaking into smaller drops in a finite time. A typical example of pinch-off is shown in Fig. 2 for density ratio $D = 2$ with the global evolution of the drop shape in Fig. 2(a) and a magnification of the pinch-off region in Fig. 2(b). This example was integrated until $R_{\min} = 1.8 \times 10^{-7}$, at which point there were 323 node points, mainly concentrated in the pinch-off region.

The global drop evolution can be described as follows. The thin waist of the initial extended drop starts necking due to capillarity acting on the azimuthal curvature. As a consequence of the asymmetry of the initial shape, the necking is more pronounced on one side and eventually turnover occurs and a double-cone structure develops with one side folded backwards upon the other with an internal angle of greater than 90°. A similar double-cone structure has previously been reported for $D = 0$ [4] and $D = 1$ [5]. After turnover occurs, the tip of the pinch-off region continues to advance towards the axis and pinch-off occurs with $R_{\min} \to 0$ in a finite time. If the initial drop shape is perfectly symmetric, then pinch-off occurs simultaneously at two symmetrically placed points producing three droplets, with the local structure of each pinching-region as described above.

We expect the approach to pinch-off to be self-similar as $\tau = t_p - t \to 0$, where t_p is the time of pinch-off and τ is the time until pinch-off. Since $\nabla^2 \phi = 0$ it follows that both the R and Z length scales must be comparable as pinch-off is approached with $R \sim Z \sim \ell$. Balancing the dynamic pressure ρu^2 with the capillary pressure σ/ℓ and estimating the velocity scale by $u \sim \ell/\tau$ leads to the similarity scaling

$$R, Z \sim \left(\frac{\sigma \tau^2}{\rho} \right)^{1/3} \qquad \text{and} \qquad \phi, \mu \sim \left(\frac{\sigma^2 \tau}{\rho^2} \right)^{1/3}, \tag{15}$$

as in [4, 5]. To examine the applicability of this scaling here, we plot $R_{\min}^{3/2}$ versus t in Fig. 3. As $R_{\min} \to 0$, the data lie on a straight line consistent with Eq. (15). The data can be extrapolated to find the pinch-off time t_p. Similarly, a graph of $Z_{\min}^{3/2}$ versus t can be extrapolated to find Z_p, the location on the Z-axis where pinch-off occurs. Having determined t_p (and hence $\tau = t_p - t$) and Z_p, the interfacial shape can be replotted near the pinch-off region using the scaled variables $R^* = R/\tau^{2/3}$ and $Z^* = (Z - Z_p)/\tau^{2/3}$, as shown in Fig. 4. There is a clear collapse of the data from over three decades of variation in $R_{\min}$ onto a single curve.

The self-similar behaviour of ϕ and μ is shown in Fig. 5 with $\phi^* = (\phi - \phi_{\min})/\tau^{1/3}$ and $\mu^* = (\mu - \mu_{\min})/\tau^{1/3}$ plotted versus $s^* = s/\tau^{2/3}$, where s is the arclength measured from the location of $R = R_{\min}$ with s^* increasing in the direction of the shallow cone, $\phi_{\min} = \phi(s = 0)$ and $\mu_{\min} = \mu(s = 0)$. Again there is excellent collapse of the data and it is found that both μ^* and ϕ^* vary as $|s^*|^{1/2}$ at large s^*. The collapse of the data in Figs. 4 and 5 is, in fact, exactly onto the similarity solutions discussed in sections 4 and 5. These similarity solutions have been plotted as lines in Figs. 4 and 5, but are largely hidden by the data points.

The results plotted in Figs. 3–5 correspond to the initial drop shape shown in Fig. 2. Pinch-off was also calculated for a number of other initial conditions with $D = 2$. In all cases, the data collapsed onto the same curves, (or, if turnover occurred in the opposite sense, their reflections) suggesting that pinch-off is indeed a locally determined phenomena, independent of initial and far-field conditions.

Time-dependent simulations were performed for many different values of the density ratio D, and evidence for self-similarity, akin to that presented in Figs. 3–5 for $D = 2$, was observed for $0 \le D \le 3.5$. The self-similar shape of the pinch-off region and the dipole-strength distribution are dependent on the density ratio. (Plots for different values of D will be presented in Section 4.) However, in the range $0 \le D \le 3.5$, the approach to pinch-off follows the same qualitative pattern: after initial necking and turnover, the nose of the pinch-off region accelerates towards the Z-axis without significant change of shape.

For larger values of D, the approach to pinch-off after turnover is somewhat different. Fig. 6 shows the interfacial shape at different times during evolution from the same initial shape for $D = 4$, 5 and 6. The most notable difference at these larger values of D is that the tip of the nose rolls upwards as the nose moves towards the Z-axis. In fact, it appears as if there are two mechanisms competing to control the dynamics of the flow. One mechanism causes the tip of the pinch-off nose to roll upwards, with this mechanism becoming more dominant as D increases, while the usual pinching mechanism draws the lower edge of the nose towards the Z-axis. This competition between roll-up and pinching is most striking for $D = 6$ [Fig. 6(c)]. In this case, the tip of the nose rolls upwards after turnover, and a second nose is formed as the lower edge of the initial nose continues to move towards the axis. The tip of this second nose is then also observed to roll up as it moves towards the

7

axis. We speculate that for $D = 6$, pinch-off is approached through a succession of such rolling/splitting events. Unfortunately, due to computational limitations, this could not be verified since more and more nodes are required to resolve the shape. The simulation for $D = 6$ was terminated when $R_{\min} = 0.0001$, at which point there were 490 nodes along the interface.

For $D = 4$, the simulation was continued to $R_{\min} = 1.0 \times 10^{-7}$ at which point there is no hint of further roll-up and it seems that self-similar pinch-off is inevitable. The limiting shape of the pinch-off region for $D = 4$ is again a double-cone structure which, as for the smaller values of D, could be collapsed using the self-similar scaling. However, the data for $D = 4$ only collapses well for $R_{\min} < 1.0 \times 10^{-5}$ since there is a significant transient during which the roll-up event influences the shape. For $D = 5$, the simulation was terminated when $R_{\min} = 1.0 \times 10^{-4}$ (using 460 nodes), at which stage it seems likely there will be another roll-up event. It is not clear whether there will be a succession of roll-up events, as perhaps for $D = 6$, or whether self-similar pinch-off will occur at much smaller values of $R_{\min}$.

The results in Fig. 6 show that the approach to pinch-off is strongly dependent on the density ratio D. Further evidence of this is provided by consideration of the variation of θ' with τ for different values of D, where

$$\theta'(\tau) = \tan^{-1}\left(\frac{dR}{ds}\Big/\frac{dZ}{ds}\right) \tag{16}$$

is the angle measured on the shallow cone at a radius $R = 10R_{\min}(t)$. This angle tends towards a constant as $\tau \to 0$, as is consistent with asymptotic self-similarity. However, as can be seen in Fig. 7, the convergence is monotonic at small values of D, but oscillatory at larger values of D. The rate of convergence can be estimated by fitting curves of the form

$$\theta' = \theta'_0 + \mathrm{Re}(c_1 \tau^{c_2 + ic_3}) , \tag{17}$$

where θ'_0, c_1, c_2, c_3 are real constants. While the fit is not well-constrained over this range of τ, the results indicate that the decay coefficient c_2 decreases monotonically as D increases, while the frequency c_3 increases. This suggests that the pinch-off process becomes less stable as the density ratio is increased, as will be confirmed in Section 6.

4 Formulation in similarity variables

The results from the time-dependent simulations suggest that pinch-off is indeed a self-similar process up to at least for $D = 4$. Thus we introduce similarity variables

$$R^* = R/\tau^{2/3}, \qquad Z^* = (Z - Z_p)/\tau^{2/3}, \qquad t^* = -\ln\tau \qquad (18)$$

and

$$\phi^* = (\phi - \phi_p)/\tau^{1/3}, \qquad \mu^* = (\mu - \mu_p)/\tau^{1/3}. \qquad (19)$$

The Bernoulli constraint in similarity variables becomes

$$-\frac{\partial\beta}{\partial t} = \left(-\frac{1}{3}\phi + \frac{2}{3}\mathbf{X}\cdot\nabla\phi + \frac{1}{2}|\nabla\phi|^2\right)^+ - D\left(-\frac{1}{3}\phi + \frac{2}{3}\mathbf{X}\cdot\nabla\phi + \frac{1}{2}|\nabla\phi|^2\right)^- + \kappa \qquad (20)$$

where we have dropped the *'s, and $\mathbf{X} = (R, Z)$ in cylindrical coordinates. The kinematic boundary condition (2) is imposed by defining $G(\mathbf{X}, t)$ to be the signed normal distance in similarity space from a point $\mathbf{X}$ to the interface so that $\nabla G = \mathbf{n}$ on the interface. Then Eq. (2) becomes

$$-\frac{\partial G}{\partial t} = \left(\frac{2}{3}\mathbf{X} + \nabla\phi\right)\cdot\nabla G. \qquad (21)$$

Eqs. (20) and (21) can be rewritten in the form

$$\frac{\partial\beta}{\partial t} = -B \qquad (22)$$

$$\frac{\partial G}{\partial t} = -K \qquad (23)$$

so that steady similarity solutions correspond to solutions of $B = K = 0$. These equations are solved discretely at N_p points along a truncated interface that represents the nose region as shown in Fig. 8. The truncated interface is extrapolated to infinity by specifying

$$\mu = \mu_0 r^{1/2} + \frac{\mu_1}{r} \qquad (24)$$

along

$$\theta = \theta_0 + \frac{\theta_1}{r^{3/2}} \qquad (25)$$

as $r \to \infty$, where (r, θ) are spherical polar coordinates defined by $r = (R^2 + Z^2)^{1/2}$ and $\theta = \tan^{-1}(R/Z)$. The truncation coefficients $\theta_0, \theta_1, \mu_0$ and μ_1 are determined on each cone

9

by the constraints that θ and μ are continuous and have continuous first derivatives at the truncation points. Eqs. (24) and (25) are the first 2 terms of the asymptotic expansion for μ and θ as $r \to \infty$ [4]. The surface is closed by adding spherical caps at infinity. The surface integrals in Eqs. (5) and (14) are evaluated using Gaussian quadrature between nodes and along the extrapolated extensions to infinity.

The roots of Eqs. (22) and (23) are determined by a modified Newton scheme. A numerical approximation to the Jacobian matrix J_1 is obtained by calculating the changes to B and K due to small perturbations of μ at each node and to small normal displacements of the interface at each node and then using central differencing. Thus

$$
J_1 = \left[\begin{array}{cc} \frac{\partial B_i}{\partial \mu_j} & \frac{\partial B_i}{\partial n_j} \\ \frac{\partial K_i}{\partial \mu_j} & \frac{\partial K_i}{\partial n_j} \end{array} \right] , \tag{26}
$$

where J_1 is a $2N_p \times 2N_p$ matrix composed of four $N_p \times N_p$ sub-matrices. The dipole strength and interfacial location are updated from the kth iterate using the modified Newton step

$$
\mu_i^{(k+1)} = \mu_i^{(k)} + \alpha \, \delta\mu_i \tag{27}
$$

$$
Z_i^{(k+1)} = Z_i^{(k)} + \alpha n_Z \, \delta n_i \tag{28}
$$

$$
R_i^{(k+1)} = R_i^{(k)} + \alpha n_R \, \delta n_i , \tag{29}
$$

where $\mathbf{n} = (n_Z, n_R)$,

$$
\left(\begin{array}{c} \delta\mu_i \\ \delta n_i \end{array} \right) = -J_1^{-1} \left(\begin{array}{c} B_i \\ K_i \end{array} \right) \tag{30}
$$

and α represents the fraction of the complete Newton step that results in the largest reduction of $\sum(B_i^2 + K_i^2)$. Iteration of (27)–(29) is performed with a given truncation distance $r = r_{\text{trunc}}$ until a convergence criterion

$$
\max(|B_i|, |K_i|) < \epsilon \tag{31}
$$

is met, where typically $\epsilon = 10^{-12}$. The extent of the nose region is then increased by adding more nodes while increasing the truncation distance $r = r_{\text{trunc}}$. This procedure is repeated until the obtained solution is independent of the truncation distance, typically with $r_{\text{trunc}} \sim 1000$. For $D = 1$, the initial guess for the Newton iteration was obtained from the time-dependent solutions, while solutions for other values of D were obtained by a continuation procedure.

10

5 Similarity solutions

Using the technique described above, we calculated similarity solutions of Eqs. (20) and (21) for varying values of the density ratio D. Where self-similar behaviour had been observed in the time-dependent simulations, there is excellent agreement with the scaled solutions (Figs. 4,5). Some further verification of our results is provided by comparison with previous studies of special cases. Inviscid pinch-off for $D = 0$ has been studied by [4] who performed time-dependent simulations similar to those described in Section 3. The similarity shape obtained by rescaling in [4] is indistinguishable from the $D = 0$ curve in Fig. 11 obtained here by Newtonian iteration. Moreover, the previous estimates 18.1° and 112.8° for the cone angles are in excellent agreement with our calculated values of 17.99° and 112.74°. The case $D = 1$ has been studied by [5] who performed time-dependent simulations down to $R_{min} \simeq 0.001$. The cone angles of self-similar pinch-off were estimated to be 12° and 127°, which differ somewhat from our calculated values of 19.85° and 120.50°. The difference is probably due to the limited range of R_{min} in [5].

Some insight into the dynamics of inviscid pinch-off is provided by Figs. 9 and 10, which show the interfacial velocities and the terms contributing to interfacial balance of pressures for $D = \frac{1}{2}$, 2 and 8. The internal and external pressures are

$$p_1 = -\left(-\frac{1}{3}\phi + \frac{2}{3}\mathbf{X} \cdot \nabla\phi + \frac{1}{2}|\nabla\phi|^2\right)^-, \tag{32}$$

and

$$p_2 = -D\left(-\frac{1}{3}\phi + \frac{2}{3}\mathbf{X} \cdot \nabla\phi + \frac{1}{2}|\nabla\phi|^2\right)^+ \tag{33}$$

respectively and the pressure balance is simply $p_1 - p_2 = \kappa$. At all values of D the positive curvature along the shallow cone drives a jet towards the pinch-off point along both sides of the interface with substantially higher velocities in the interior (Fig. 9). The internal velocities increase towards the tip as the fluid flows through the narrow gap at the pinch-off point. The large internal velocities lead to a large negative internal pressure (Fig. 10) with the result that the pinching region is sucked towards the axis by the Bernoulli effect. The internal jet rapidly decelerates along the steep cone as the flow expands away from the constriction in the pinching region. The flow in the external fluid is towards the tip along the

11

steep cone, in order to provide the necessary fluid to advance the tip. As D increases, the fluid velocities increase on both sides of the interface, although the locations of the velocity peaks remain approximately the same. The magnitude of the external pressure also increases as D increases, primarily due to the linear dependence of p_2 on D. For the case of $D = 0$ there is necessarily an exact balance between the internal pressure and surface tension. As D becomes large, the external pressure becomes increasingly significant in the pressure balance.

Similarity solutions were found over the range $0 \leq D \leq 11.8$, and the results are shown in Figs. 11–13. Fig. 11 plots the similarity shapes of the interface for various values of D, while Figs. 12 and 13 plot the leading-order coefficients of the far-field cone angles and dipole strengths, respectively, as functions of D. The similarity shapes vary markedly with D and the interface bends further back upon itself as D is increased. As can be seen in Fig. 12, the shallow cone angle is relatively insensitive to changes in D, whereas the steep cone angle increases markedly with D over the range $0 \leq D < 6$ before it too becomes relatively insensitive to changes in D. Another observation from Fig. 11 is that the nose of the interface is displaced to the right in similarity variables as D increases, corresponding to an increase in the axial velocity of the nose. Fig. 13 shows that the far-field dipole strength along the shallow cone varies little with D, while the dipole strength along the steep cone increases approximately linearly with D.

The smooth variations observed in Figs. 11–13 as D increases give no indication that that similarity solutions cease to exist for $D > 11.8$. However, we were unable to obtain such solutions by continuation because the smallest eigenvalue of the Jacobian matrix J_1 vanishes as $D \rightarrow 11.8$ (Fig. 14), the Jacobian matrix becomes singular and our Newton iteration scheme fails. Attempts to jump over this value of D failed to converge to smooth solutions, perhaps because of poor initial guesses for the Newton iteration. We speculate that there is a branch of steady similarity solutions in $D > 11.8$ but did not invest further effort to find it since, as the stability analysis in Section 6 demonstrates, the steady similarity solutions are unstable to time-dependent perturbations for $D > 6.2$ and hence will not be observed physically.

12

6 Stability Analysis

The stability of the similarity solutions discussed above is determined by examining the eigenspectrum of the Jacobian matrix

$$J_2 = - \begin{bmatrix} \frac{\partial B_i}{\partial \beta_j} & \frac{\partial B_i}{\partial G_j} \\ \frac{\partial K_i}{\partial \beta_j} & \frac{\partial K_i}{\partial G_j} \end{bmatrix}, \tag{34}$$

which describes the linearized dynamics of (22) and (23) about a solution $B_i = K_i = 0$. This Jacobian can be found numerically using the variable transformation

$$J_2 = - \begin{bmatrix} \frac{\partial B_i}{\partial \mu_j} & \frac{\partial B_i}{\partial n_j} \\ \frac{\partial K_i}{\partial \mu_j} & \frac{\partial K_i}{\partial n_j} \end{bmatrix} \begin{bmatrix} \frac{\partial \mu_i}{\partial \beta_j} & \frac{\partial \mu_i}{\partial G_j} \\ \frac{\partial n_i}{\partial \beta_j} & \frac{\partial n_i}{\partial G_j} \end{bmatrix} = -J_1 \begin{bmatrix} \frac{\partial \beta_i}{\partial \mu_j} & \frac{\partial \beta_i}{\partial n_j} \\ \frac{\partial G_i}{\partial \mu_j} & \frac{\partial G_i}{\partial n_j} \end{bmatrix}^{-1},$$

calculating the $N_p \times N_p$ derivative matrices $\partial \beta_i / \partial \mu_j$ and $\partial \beta_i / \partial n_j$ using central differences, and noting that $\partial G_i / \partial \mu_j = 0$ and $\partial G_i / \partial n_j = I$ due to the definition of G.

The eigenvalues and associated eigenvectors of J_2 were calculated using NAG routine F02AGF for all values of D for which similarity solutions were obtained. For a given numerical discretization there are $2N_p$ eigenmodes. Some of these were found to *vary strongly* ←
with the nodal spacing and had highly oscillatory eigenvectors that were clearly not resolved representations of the true dynamics. These modes were discarded as artifacts of discretization, and the numerical results presented below refer to the remaining eigenmodes, which appear to be robustly determined and hence are assumed to correspond to the dynamics of the continuous system.

As in [9], we note that, while most continuous eigenmodes correspond to the dynamics of approach to a steady similarity solution, some simply correspond to the three degrees of freedom associated with the definition of the similarity variables in Eqs. (18) and (19). A shift in the origin of the dipole potential of the form $\mu_p \rightarrow \mu_p + \epsilon$ introduces an eigenmode with $\mathbf{e}_\beta = 1$, $\mathbf{e}_n = 0$ and eigenvalue $\lambda_\mu = \frac{1}{3}$; a shift in the location of the pinch-off point $Z_p \rightarrow Z_p + \epsilon$ introduces an eigenmode with $\mathbf{e}_\beta = \beta_s Z_s$, $\mathbf{e}_n = R_s$ and eigenvalue $\lambda_z = \frac{2}{3}$ (where subscript s refers to a tangential derivative); and a shift in the time origin with $t_p \rightarrow t_p + \epsilon$ introduces an eigenmode with $\mathbf{e}_\beta = \frac{1}{3}\beta - \frac{2}{3}\beta_s(RR_s + ZZ_s)$, $\mathbf{e}_n = RZ_s - ZR_s$ and eigenvalue $\lambda_t = 1$. These eigenmodes do not represent genuine instabilities even though

13

the associated eigenvalues have positive real parts. Rather, they indicate that solutions with slightly different pinch-off times, pinch-off locations, and dipole-potential origins, will appear to diverge exponentially in similarity space.

In all cases eigenmodes corresponding to $\lambda_\mu = \frac{1}{3}$, $\lambda_z = \frac{2}{3}$ and $\lambda_t = 1$ were observed in the eigenspectrum of the numerical discretization J_2. Fig. 15 plots the three eigenvectors as a function of arclength s for $D = 1$. The points correspond to suitably rescaled eigenvectors of J_2 and the solid lines to the analytic predictions above. There is excellent agreement between the discrete and continuous systems. The corresponding numerically determined eigenvalues are $\lambda_\mu = 0.3333$, $\lambda_z = 0.6693$ and $\lambda_t = 0.9995$, again in excellent agreement with the analytic predictions for the continuous system.

For $0 \leq D \leq 6.2$ all the other robustly determined numerical eigenvalues had negative real parts indicating stable similarity solutions. For $D < 2.1$ the least stable eigenvalue was real, and in $2.1 < D < 6.2$ the least stable eigenvalues were a complex conjugate pair. When $D \approx 6.2$ a Hopf bifurcation occurs with the complex conjugate pair passing from the left-hand half plane to the right-hand half plane. Far from the nose the complex eigenvectors obey

$$\mathbf{e}_\mu \propto s^{(1-3\lambda)/2}, \qquad \mathbf{e}_n \propto s^{1-3\lambda/2}, \tag{35}$$

which corresponds to a dynamically passive far-field disturbance that is left behind by an oscillatory instability at the advancing nose (Fig. 16). Further work is required to understand the physical mechanism of this instability.

The results of this stability analysis illuminate and are consistent with the results from the time-dependent simulations presented in Figs. 6 and 7, which showed that the approach to pinch-off becomes first oscillatory near $D = 2$ and then progressively less stable as D is increased towards $D = 6$. Though the behaviour of θ' for $D = 4$ has clearly not settled fully to the form (17), the value $c_3 = 1.5$ estimated from the oscillation is reasonably close to the value $Im(\lambda) = 1.1$ obtained for the slowest decaying eigenmode from the stability analysis.

Though the stability analysis shows that the steady solution branch is unstable for $D > 6.2$, it is of some interest to note the form of the eigenvector corresponding to the stationary bifurcation at $D = 11.8$ (Fig. 17). While the oscillatory instability at $D = 6.2$ corresponds to the nose shaking from side to side, the instability at $D = 11.8$ corresponds to a tilting of

14

the interfacial shape. Before I got a sharpening or blunting of the nose.

7   Conclusions

In this paper we have used a boundary-integral formulation to examine the effect of density ratio on the pinch-off of inviscid drops. This study extends the work of [4] and [5] on density ratios $D = 0$ and $D = 1$, by examining pinch-off over the range $0 \leq D < 11.8$ and analysing the stability of self-similar behaviour. Time-dependent simulations and stability analysis show that self-similar pinch-off is stable for $D < 6.2$. While our numerical technique allowed us to continue the steady branch of similarity solutions into the range $6.2 < D < 11.8$ where they are unstable to oscillatory solutions, we were unable to find similarity solutions for $D > 11.8$ owing to a stationary bifurcation.

The self-similar solutions are all characterized by a double-cone interfacial structure with one cone folding back over the other with an internal angle of greater than 90°. Capillarity acts on the large azimuthal curvature of the shallow cone to drive a jet of fluid towards the pinch-off point. Large internal fluid velocities generate a low internal pressure and Bernoulli suction pulls the tip of the pinch-off region towards the axis. As D increases, the internal angle between the double cones decreases and the fluid velocities on each side of the interface increase. It is possible that these higher fluid velocities trigger the observed instability at $D = 6.2$. More work is required to investigate the exact nature of this instability.

Where self-similarity obtains, both the far-field cone angles and the far-field flow are uniquely determined by the density ratio D (Figs. 12,13). These values function as prescribed initial conditions for the recoil of the interface after pinch-off. Calculations for the post pinch-off problem, showing that these conditions are necessary and sufficient, will be presented elsewhere [Sierou & Lister, in preparation]. It is an open question how pinch-off is attained for $D > 6.2$ when the steady similarity solutions are unstable. Time-dependent calculations typically show tendrils of one fluid being pulled into the other as necking develops, perhaps driven by a Kelvin–Helmholtz type of instability acting on the interfacial shear. The computational cost required to resolve the high curvature of these tendrils becomes prohibitive before pinch-off is approached.

A Verification of the numerical scheme

The numerical implementation of (5) and (14) was verified using the analytic test case

$$\left.\begin{array}{l} \mu = P_m(\cos(s)) \\ Z = -\cos(s) \\ R = \sin(s) \end{array}\right\} \quad \text{for} \quad 0 \le s \le \pi, \tag{36}$$

where P_m is the Legendre polynomial of order m, which has the solution

$$\overline{\phi} = \frac{1}{4m+2}P_m(\cos(s)), \qquad \frac{\partial \overline{\phi}}{\partial n} = -\frac{m(m+1)}{2m+1}P_m(\cos(s)). \tag{37}$$

The difference between the numerical and analytical results showed sixth-order convergence in the nodal spacing, consistent with the use of quintic splines.

The time-stepping algorithm was tested by simulating the oscillation of inviscid drops. According to linear theory [8], if a spherical drop is perturbed such that

$$\left.\begin{array}{l} \mu = 0 \\ Z = -\cos(s)\{1 + \epsilon P_m(\cos(s))\} \\ R = \sin(s)\{1 + \epsilon P_m(\cos(s))\} \end{array}\right\} \quad \text{for} \quad 0 \le s \le \pi \tag{38}$$

at $t = 0$, with $\epsilon \ll 1$, then the drop oscillates with frequency ω given by

$$\omega^2 = \frac{m(m-1)(m+1)(m+2)}{Dm + (m+1)}. \tag{39}$$

Simulations were performed for $m = 2, 3, 4$, with $\epsilon = 0.05$ using $N_p = 65$ nodes for values of D in the range $0 \le D \le 20$. In all cases the observed frequencies were within 0.2% of the analytical results.

References

[1] J. Eggers, Universal pinching of 3D axisymmetric free-surface flow, *Phys. Rev. Lett.*, **71**(21), 3458–3460 (1993).

[2] D. Papageorgiou, On the breakup of viscous liquid threads, *Phys. Fluids*, **7**, 1529–1544 (1995).

[3] M. P. Brenner, J. R. Lister, and H. A. Stone, Pinching threads, singularities and the number 0.0304 ..., *Phys. Fluids*, **8**(11), 2827–2836 (1996).

[4] R. F. Day, E. J. Hinch, and J. R. Lister, Self-similar capillary pinchoff of an inviscid fluid, *Phys. Rev. Lett.*, **80(4)**, 704–707 (1998).

[5] Y. -J. Chen, and P. H. Steen, Dynamics of inviscid capillary breakup: collapse and pinchoff of a film bridge, *J. Fluid. Mech.*, **341**, 245–267 (1997).

[6] J. Eggers, Nonlinear dynamics and breakup of free-surface flows, *Rev. Mod. Phys.*, **3**, 865–929 (1997).

[7] Q. Nie and G. Baker, Application of adaptive quadrature to axisymmetric vortex sheet motion, *J. Comp. Phys.*, **143**, 46–69 (1998).

[8] H. Lamb, *Hydrodynamics*, Cambridge University Press, Cambridge (1932).

[9] T. P. Witelski and A. J. Bernoff, Stability of self-similar solutions for van der Waals driven thin film rupture, *Phys. Fluids.* **11(9)**, 2443–2455 (1999)
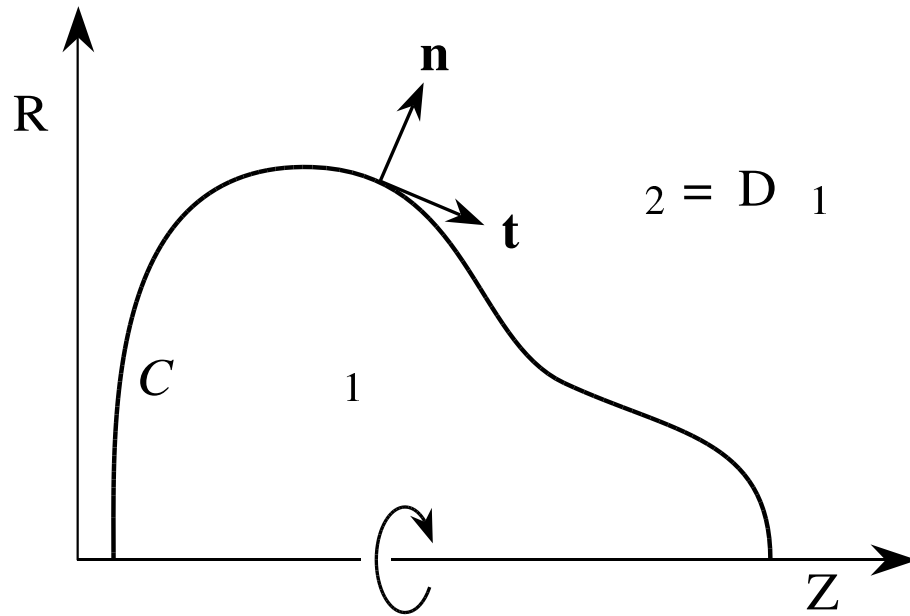
Figure 1: The cylindrical co-ordinate system used to represent an axisymmetric interface S obtained by rotating the curve C about the Z-axis. The density ratio $D = \rho_2/\rho_1$.
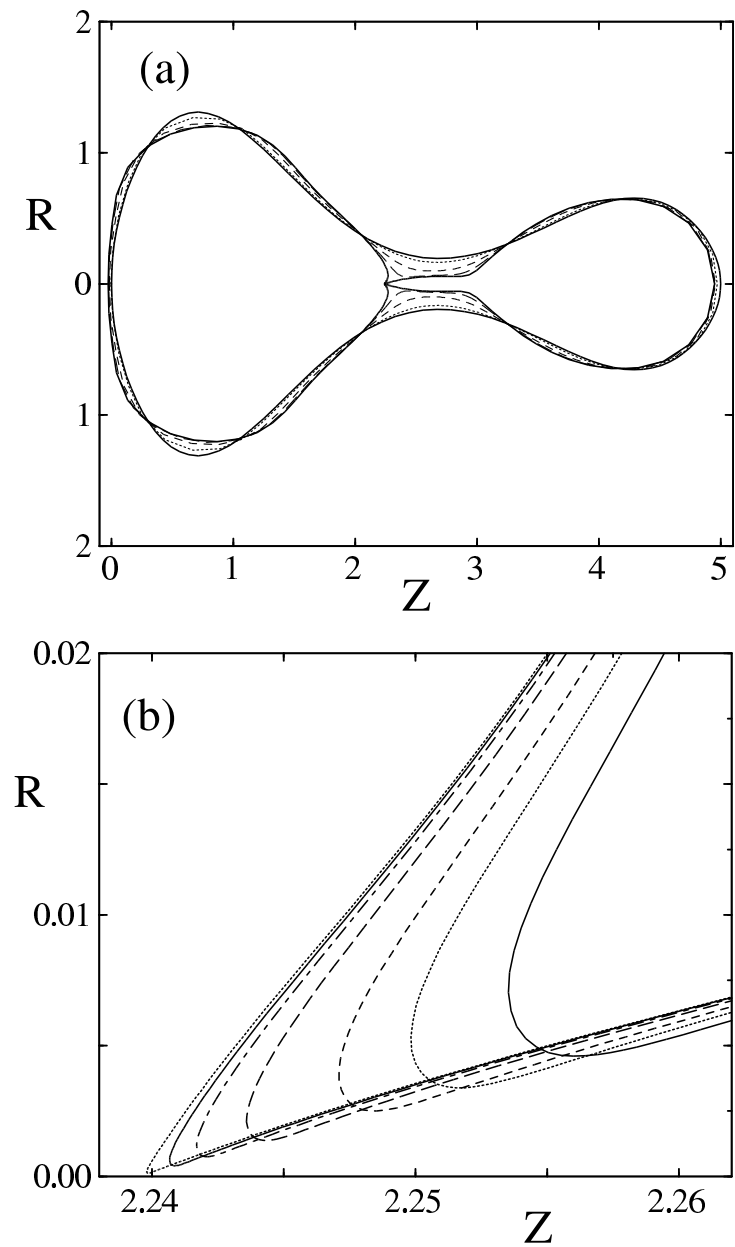
Figure 2: Time-dependent pinch-off of a drop with $D = 2$. (a) Global evolution from an initial shape given by the curve with the widest waist. (b) Magnification of the pinch-off region. The different curves correspond to different times.
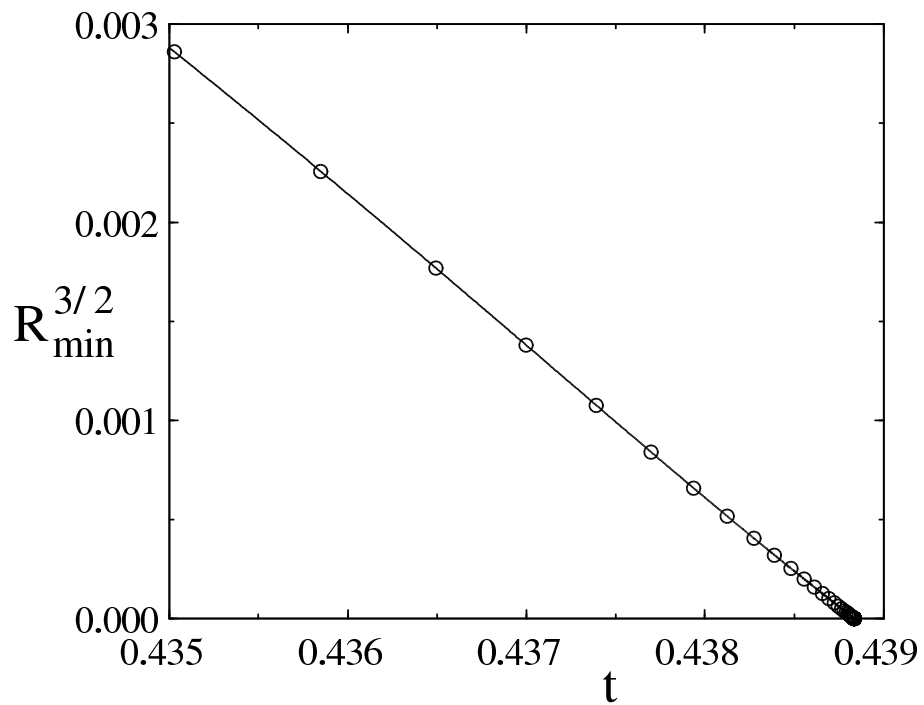
Figure 3: The approach to pinch-off for $D = 2$ confirms the scaling $R_{\min} \sim \tau^{2/3}$ as pinch-off time $\tau = t_p - t \to 0$.
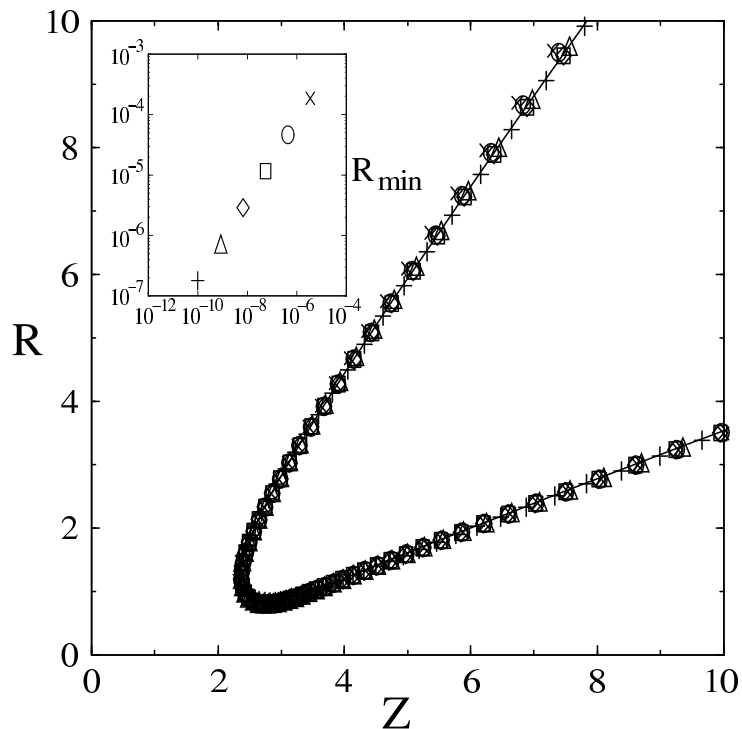
Figure 4: The collapse of the scaled interfacial shapes for $D = 2$ from over three decades of variation in $R_{\min}$. The inset key shows the corresponding values of $R_{\min}$ and the time until pinch-off τ. The underlying curve is the similarity solution calculated in Section 5.
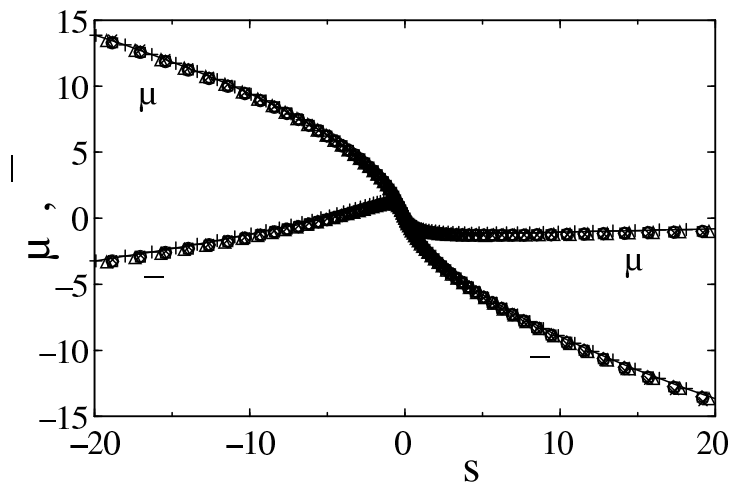
Figure 5: The self-similar collapse of μ and $\overline{\phi}$ as $\tau \to 0$ for $D = 2$. The scaled dipole strength μ^*, potential $\overline{\phi}^*$ and arclength s^* are defined in the text, and the symbols are described in the key to Fig. 4

21
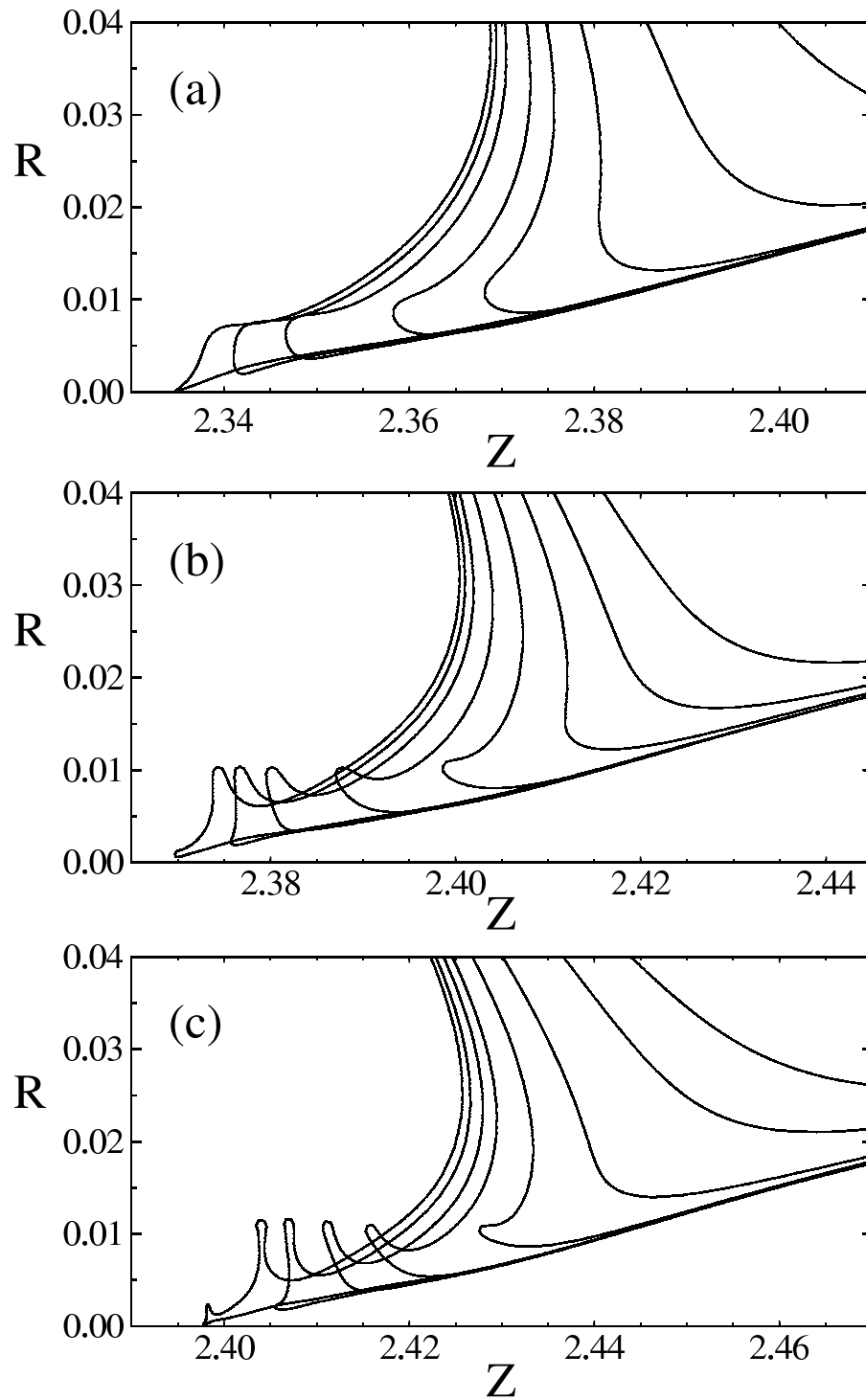
Figure 6: Time-dependent pinch-off of a drop for: (a) $D = 4$; (b) $D = 5$; (c) $D = 6$.
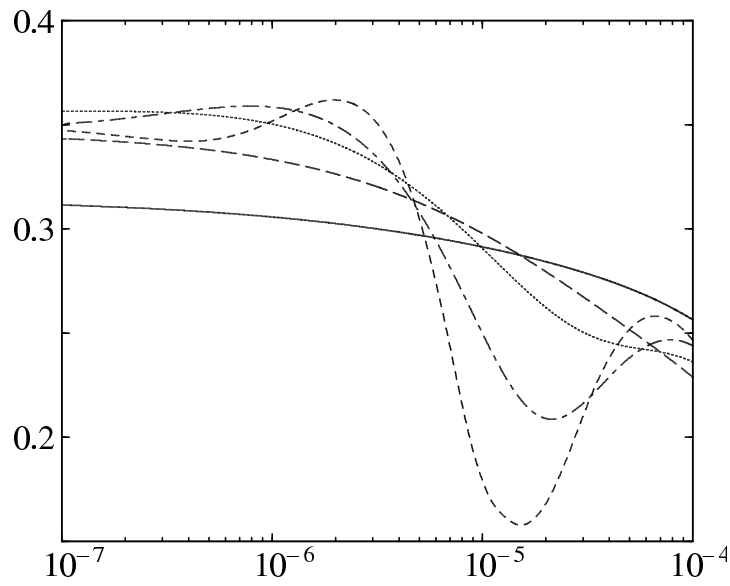
Figure 7: Slope $\theta' = \tan^{-1}(dR/dZ)$ on the shallow cone at $R/R_{\min} = 10$ versus the time until pinch-off τ for $D = 0$ (solid); $D = 1$ (long-dashed); $D = 2$ (dotted); $D = 3$ (dot-dashed); $D = 4$ (dashed). Convergence is slower and more oscillatory as D increases.
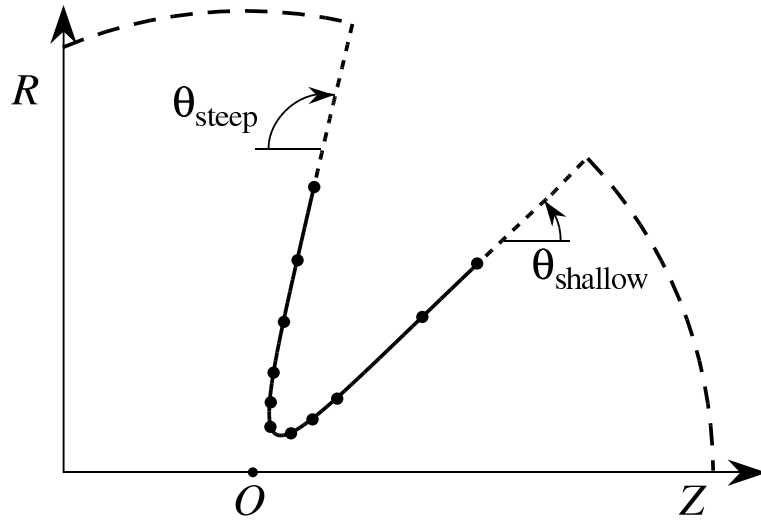
Figure 8: The truncation of the interface used to solve the similarity equations by Newton's method. The points indicate nodes used to represent the solution along the pinching nose. The short-dashed lines indicate the analytical extrapolation to infinity using Eq. (25) and the long-dashed curves represent spherical caps at infinity.

23
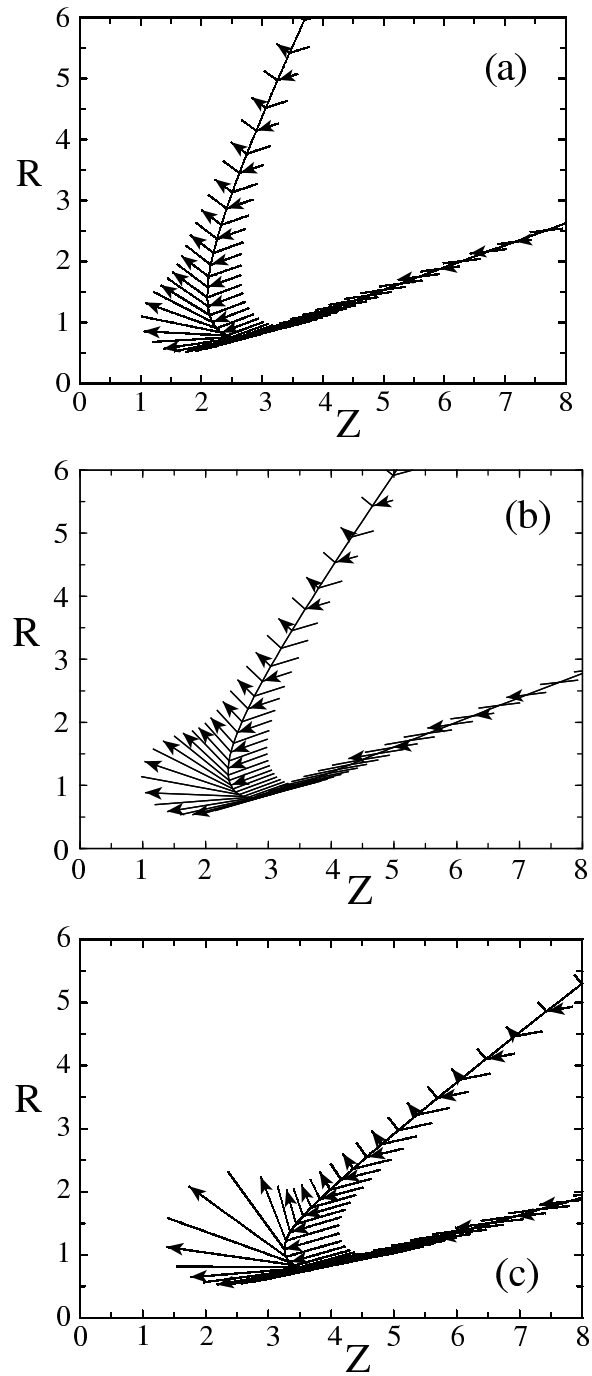
Figure 9: Plots of the interfacial velocity field for (a) $D = \frac{1}{2}$, (b) $D = 2$ and (c) $D = 8$. Vectors beginning (ending) at the interface correspond to velocities just interior (exterior) to the interface.
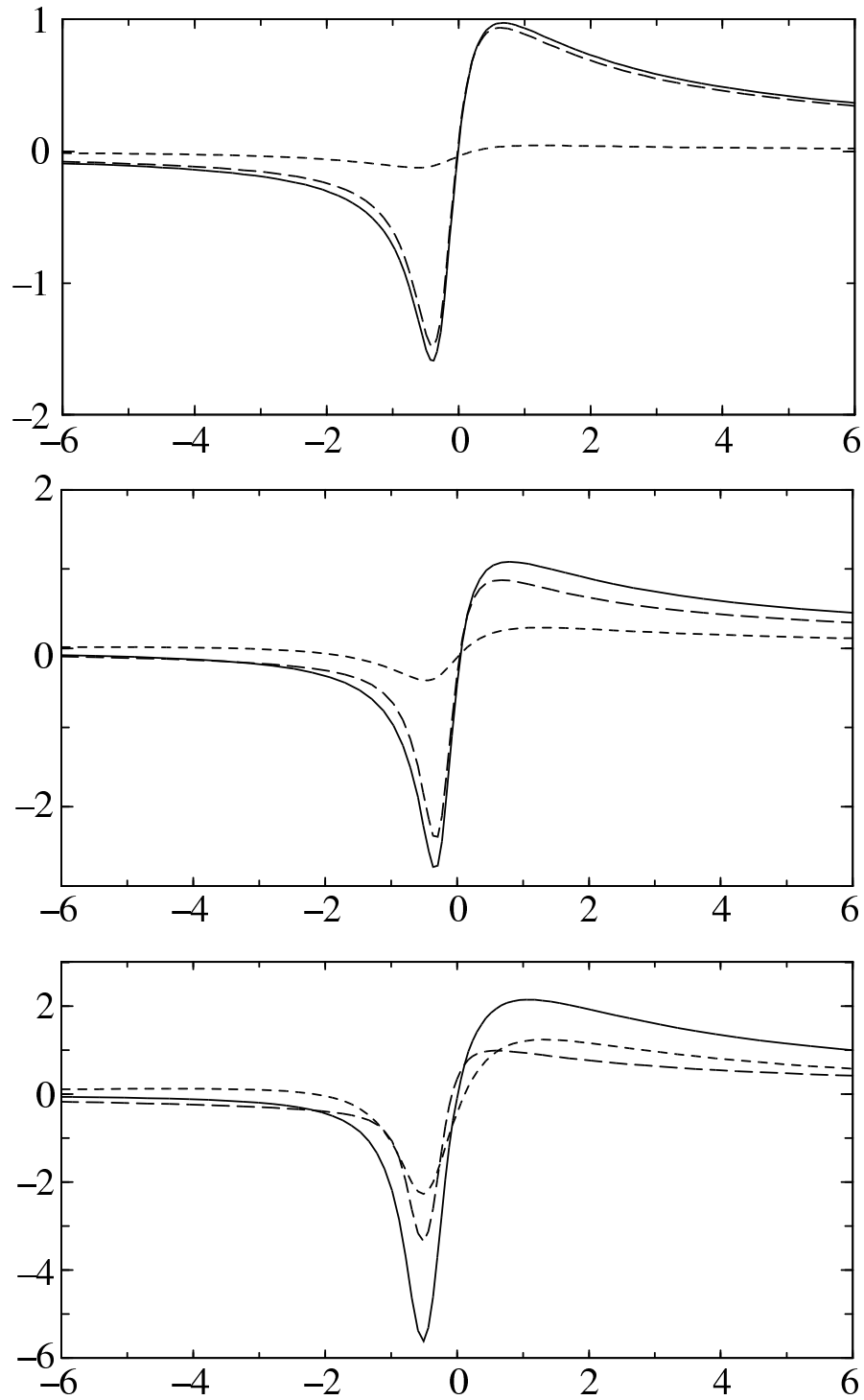
Figure 10: The Bernoulli balance $\kappa = p_1 - p_2$ for (a) $D = \frac{1}{2}$, (b) $D = 2$ and (c) $D = 8$: κ (solid); p_1 (long-dashed); p_2 (short-dashed). 25
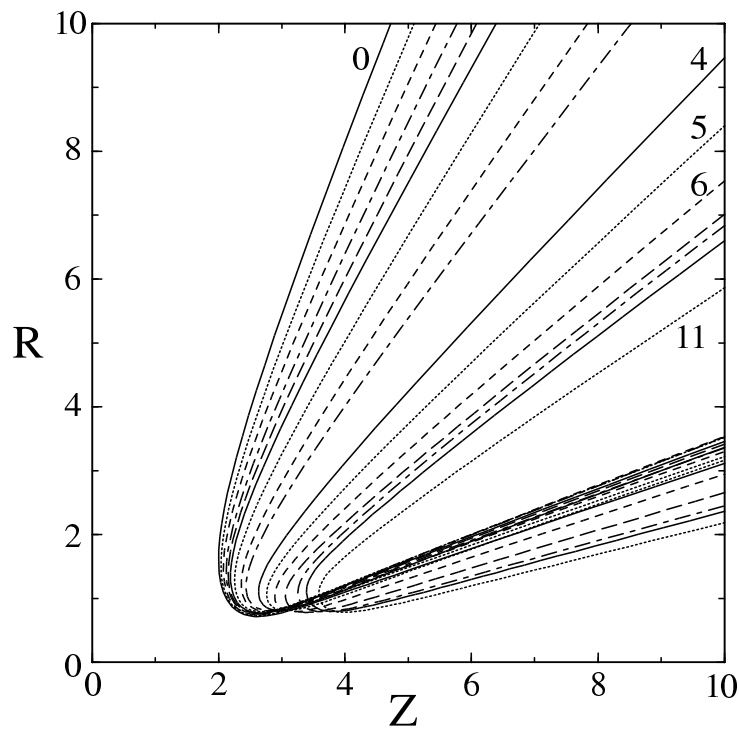
Figure 11: The shape of the similarity interface for different values of the density ratio D: $D = 0$, 0.2, 0.4, 0.6, 0.8, 1, 1.5, 2, 2.5, 4, 5, 6, 7, 8, 9 and 11 when looking from left to right from the top of the figure.
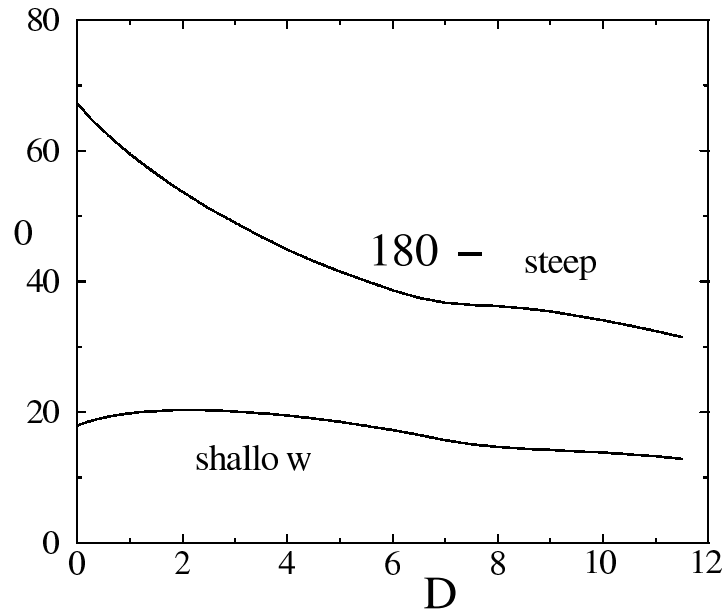
Figure 12: The leading-order coefficient θ_0 of the cone angles as a function of D.

26
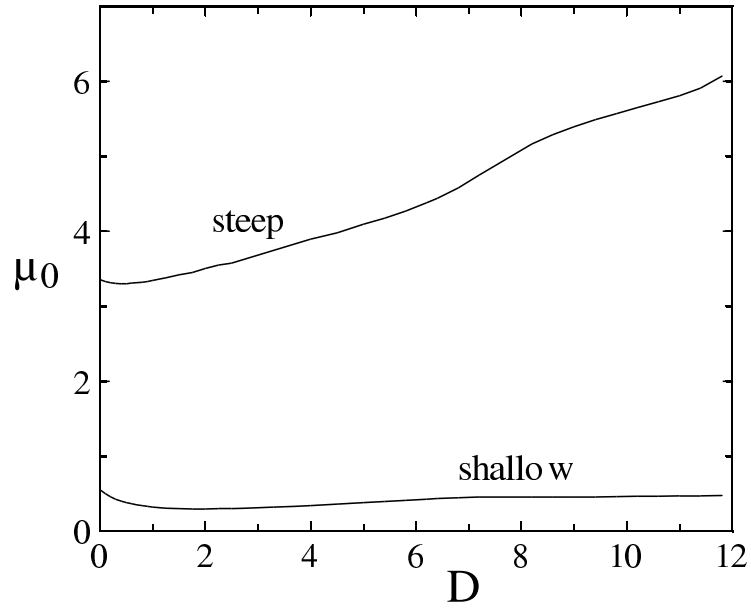
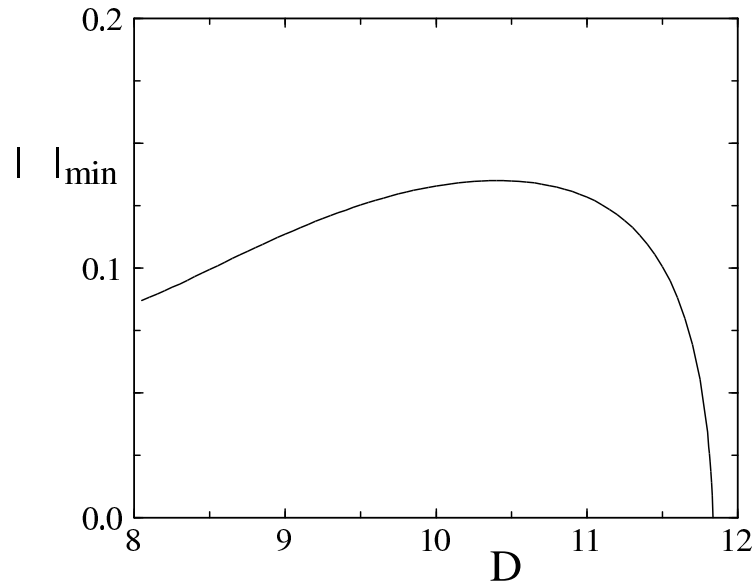Figure 13: The leading-order coefficient μ_0 of the dipole potential as a function of D.

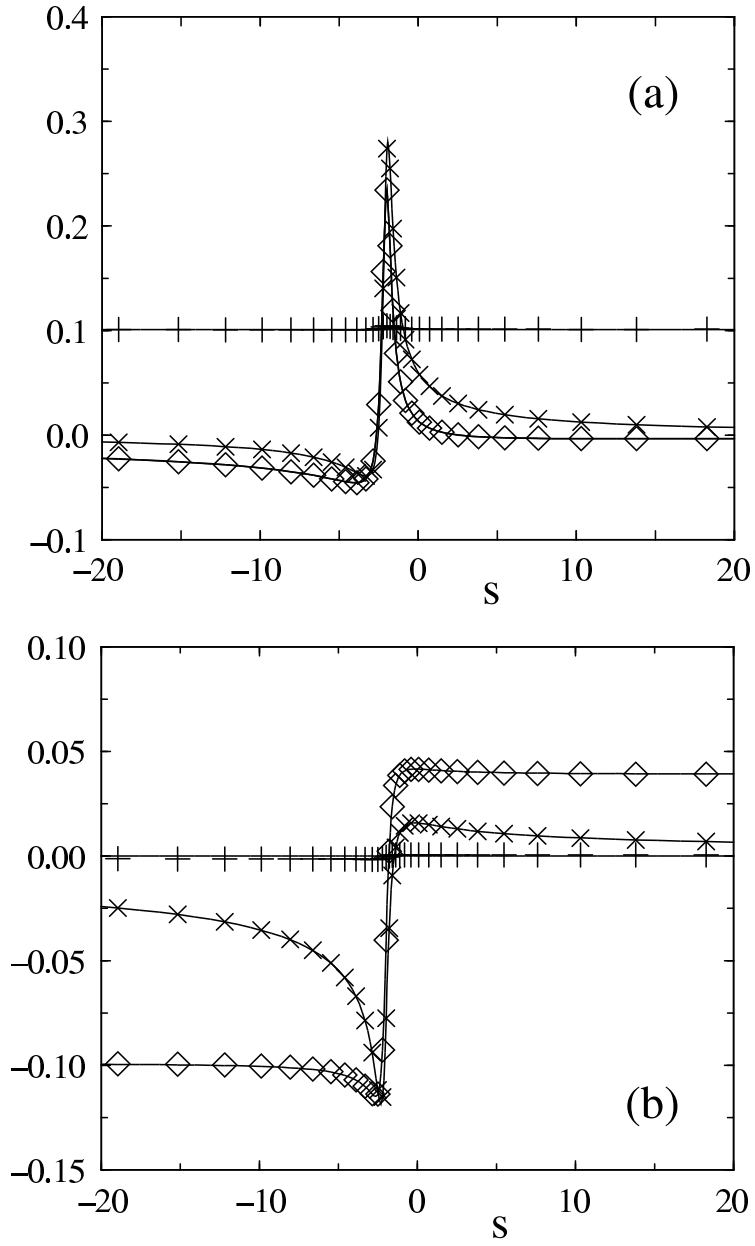Figure 14: The size of the smallest eigenvalue $|\lambda|_{\min}$ of J_1 versus density ratio D.

27

Figure 15: The eigenmodes for $D = 1$ associated with a shift in the pinch-off time ($\times$), the pinch-off location ($\diamond$), and the dipole potential($+$): (a) $\mathbf{e}_\beta$; (b) $\mathbf{e}_n$.
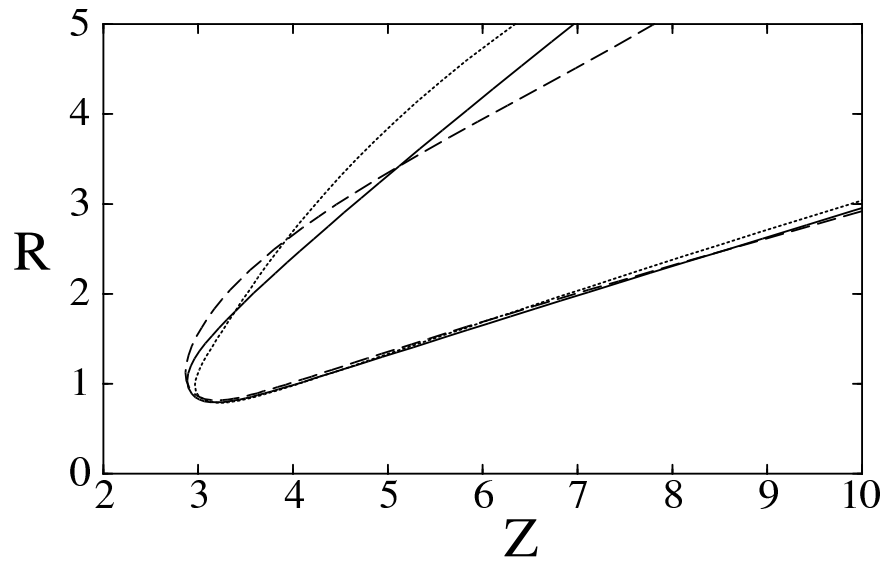
Figure 16: The eigen-perturbation to the interfacial shape (solid) at $D = 6.25$, shown with an arbitrary amplitude, real part dashed and imaginary part dotted, corresponding to a Hopf bifurcation with eigenvalue $\pm 1.5i$. The perturbation takes the form of an oscillation of the tip that leaves waves of the form (35) behind on the far-field double cone.
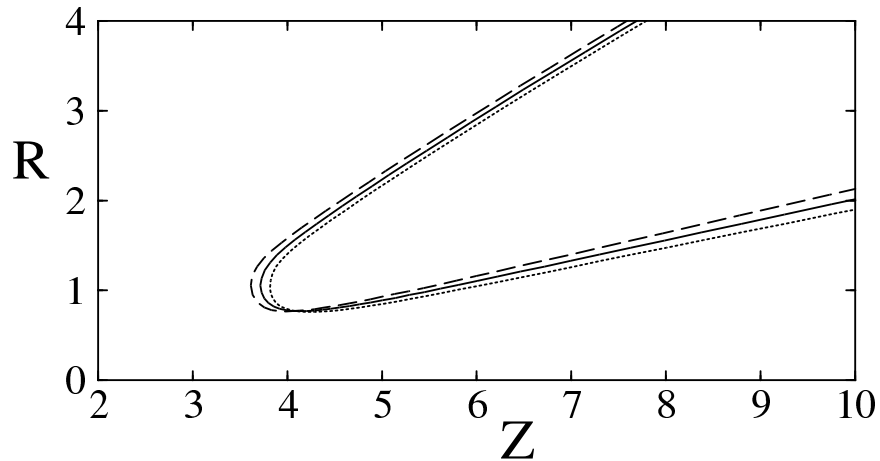

Figure 17: The stationary eigen-perturbation to the interfacial shape (solid) at $D = 11.812$, shown with two signs for the arbitrary amplitude (dashed and dotted). The eigenvalue moves into the right-half plane as D increases further to give an instability, but the oscillatory instability that set in as a Hopf bifurcation at $D = 6.2$ has eigenvalue $2.7 \pm 2.9i$ at $D = 11.8$ and is still the most unstable mode.

29